A ZVS Pulsewidth Modulation Full-Bridge Converter With a Low-RMS-Current Resonant Auxiliary Circuit

Alireza Safaee, *Senior Member, IEEE*, Praveen Jain, *Fellow, IEEE*, and Alireza Bakhshai, *Senior Member, IEEE*

***Abstract*—This paper presents the description and analysis of a phase-shift-modulated full-bridge converter with a novel robust passive low-rms-current resonant auxiliary circuit for zero-voltage switching (ZVS) operation of both the leading and lagging switch legs. Detailed time-domain analysis describes the steady-state behavior of the auxiliary circuit in different operating conditions. An in-depth comparative study between a fully specified baseline converter and the equivalent converter using the proposed resonant auxiliary circuit is presented. For a similar peak auxiliary current to ensure ZVS operation, a minimum of 20% reduction in rms current is obtained, which decreases the conduction losses. Key characteristics and design considerations are also fully discussed. Experimental results from a 750-W prototype confirm the predicted enhancements using the proposed resonant auxiliary circuit.**

***Index Terms*—DC–DC converter, full-bridge converter, passive auxiliary circuit, resonant auxiliary circuit, zero-voltage switching (ZVS).**

NOMENCLATURE

A	Leading leg ac node label
B	Lagging leg ac node label
v_A	Leading leg ac voltage
v_B	Lagging leg ac voltage
φ	Phase shift angle between v_A and v_B
v_{AB}	Full-bridge ac voltage
$t_{v_{\rm A}\nearrow}, t=0$	The rising edge moment of v_A
$t_{v_{\rm B}\nearrow}, t_1$	The rising edge moment of v_B
t_d	Deadtime
$I_{A\_v_{\rm A}\nearrow}$	Currents leaving node A at $t_{v_{\rm A}\nearrow}$
$I_{B\_v_{\rm B}\nearrow}$	Currents leaving node B at $t_{v_{\rm B}\nearrow}$
$V_{\rm in}$	Input dc voltage
$V_{\rm out}$	Output dc voltage
V_D	Rectifier diode voltage drop
n	Transformer turns ratio
$L_{\rm leak}$	Transformer leakage inductance (Primary)
L_m	Inductance in parallel to the primary terminals of the transformer
$L_{\rm out}$	Output filter inductor
$C_{\rm out}$	Output filter capacitor
S_{1U}, S_{1L}	Switches in the leading leg
S_{2U}, S_{2L}	Switches in the lagging leg
T	Switching period
$f_{\rm SW}$	Switching frequency
$\omega_{\rm SW}$	Switching angular frequency
L_S	Series inductor in proposed resonant auxiliary
L_P	Parallel inductor in proposed resonant auxiliary
L	Value of L_S and L_P
C_P	Capacitor in proposed resonant auxiliary
C	Value of C_P
C_{sb}	Sum of charge equivalent capacitors of S_{1L} and S_{1U} plus the stray capacitance of the transformer seen at the primary.
ω_0	Resonant frequency of proposed resonant auxiliary
Z_0	Characteristic impedance of proposed resonant auxiliary
γ	Dimensionless ratio of ω_0 and $2\omega_{\rm SW}$
$I_{L_m\_0}$	Current in L_m, at $t=0$
$I_{L_m\_H_k}$	kth harmonic of current in i_{L_m}
$I_{L_m\_{\rm rms}}$	rms value of i_{L_m}
$I_{L_S\_0}$	Current in L_S, at $t_{v_{\rm A}\nearrow}$
$I_{L_P\_0}$	Current in L_P, at $t_{v_{\rm A}\nearrow}$
$V_{C_P\_0}$	Voltage across C_P, at $t_{v_{\rm A}\nearrow}$
$I_{L_S\_1}$	Current in L_S, at $t_{v_{\rm B}\nearrow}$
$I_{L_P\_1}$	Current in L_P, at $t_{v_{\rm B}\nearrow}$
$V_{C_P\_1}$	Voltage across C_P, at $t_{v_{\rm B}\nearrow}$
$I_{\rm base}$	Absolute value of $I_{L_S\_0}$ at $\omega_{\rm SW}=\omega_0/2$ and $\gamma=1$
$I_{L_S\_H_k}$	kth harmonic of current in $L_{\rm S1}$
$I_{L_S\_{\rm rms}}$	rms value of i_{L_S}
$P_{\rm out\_nom}$	Nominal output power
$V_{\rm out\_nom}$	Nominal output voltage
ESR	Equivalent series resistance
ESL	Equivalent series inductance
EMI	Electromagnetic interference
ZVS	Zero-voltage switching

Manuscript received May 4, 2015; revised July 17, 2015; accepted August 18, 2015. Date of publication August 26, 2015; date of current version January 7, 2016. Recommended for publication by Associate Editor G. Moschopoulos.

A. Safaee was with the Department of Electrical and Computer Engineering, ePOWER, Queens University, Kingston, ON K7L 3N6 Canada. He is now with OSRAM Sylvania, Beverly, MA 01915 USA (e-mail: az_safaee@ieee.org).

P. Jain and A. Bakhshai are with the Department of Electrical and Computer Engineering, ePOWER, Queens University, Kingston, ON K7L 3N6 Canada (e-mail: praveen.jain@queensu.ca; alireza.bakhshai@queensu.ca).

Color versions of one or more of the figures in this paper are available online at http://ieeexplore.ieee.org.

Digital Object Identifier 10.1109/TPEL.2015.2473822

I. INTRODUCTION

DC/DC converters based on the full-bridge topology are widely accepted for medium power range (1–10 kW) because of many advantages: the structure is simple and symmetric, which provides the ac-voltage waveform with its peak equal to dc-side voltage level (i.e., higher power for the same ac current for example in comparison with half-bridge topology); the voltage stress across the switches is clamped to dc level; full

utilization of all switches is possible (by having similar conduction times and similar rms currents in all the switches based on the selected modulation scheme); it is possible to shrink the transformer size by optimal use of magnetic flux in both directions (i.e., letting the magnetic flux in the transformer swing between $-B$ and $+B$ around the origin of the core material B–H curve where the permeability is highest); high power density and low electromagnetic interference (EMI) are achievable; and there are various commercial integrated switch modules to choose from with proven reliability records [1]–[3].

For efficient and reliable high-frequency operation of a full-bridge converter, the soft switching of switches at both turn-on and turn-off moments should be guaranteed. At higher load levels having zero-voltage switching (ZVS) for all the switches is possible provided that the energy in the transformer leakage inductance (or an additional series inductor) be sufficient to charge/discharge the switch output capacitor in the selected deadtime [4]. At light-load conditions, however, the switches in the leading leg will lose their ZVS because of the insufficient energy stored in the leakage inductance, leading to low efficiency and high EMI due to hard switching. At lighter loads ZVS cannot be maintained for the lagging leg as well. Selecting the transformer leakage inductance large enough to ensure ZVS results in the necessity of lower primary/secondary turns ratio in the transformer and thus higher currents through the switches and lower efficiency. It also increases the transformer size and the required insulation levels due to the possibility of high voltages across the leakage inductance, and still at very light loads or no-load situations, ZVS is not maintainable [5].

Various approaches have been studied to maintain the soft switching of full-bridge converters. In [6] and [7], the transformer is modified and passive components are added on the load side. Passive auxiliary circuits are added to the output filter stage in [8] and [9]. A secondary-side switch is applied in [10]–[12]. There are solutions using modified primary as well: In [13] and [14], a coupled inductor is placed between the bridge and the transformer. There is an auxiliary transformer in [15] to carry the primary side current using two fast diodes for clamping. The primary of the transformer in [16] is clamped, and there are coupled inductors interfacing the bridge and the transformer. In [17]–[19], two power transformers are applied. In [20], soft switching is achieved by extra passive components in between the bridge and the transformer. ZVS is maintained in [21] without passing the entire current through an auxiliary circuit. There are also methods using active auxiliary circuits on primary side such as in [22] with one extra switch in [23]–[25] with two switches.

A robust method based on solely passive components is suggested in [5] and later in [26] with one auxiliary circuit per switch leg, as shown in Fig. 1. Integrating the square shape voltage waveforms, the currents in the auxiliary inductors are nearly triangular, with peak values proportional to the input voltage. The integration interval is the half period, so it is possible to adaptively select the switching frequency to control the peak current in the auxiliary circuits. The peak current in each auxiliary happens just before the deadtime in that leg. During the deadtime, the auxiliary current helps charging/discharging the

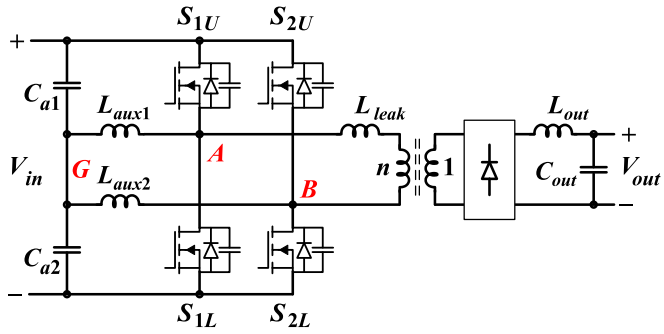

Fig. 1. Full-bridge converter with two single-inductor auxiliary circuits, one per switch leg [5].

snubber capacitors such that the next switch can turn on under ZVS condition. After the transition till the next transition half a period later the auxiliary current has no desirable function and only contributes to the conduction losses [27]. Therefore, it is desirable to have the needed peak current with the minimum rms current. A resonant auxiliary circuit providing the required peak current with lower rms current (compared to the triangular waveform) is reported in [28]–[30].

The auxiliary circuits in [5] and [26]–[30] have peak currents as a function of dc voltage and switching frequency but independent of the phase shift. The solutions in [13] and [14] as well as in [24] and [31] allow better peak current control by adding the phase shift as another control variable (although it is not fully independent).

The present paper introduces a resonant auxiliary circuit that: 1) provides the desirable peak current value for ZVS operation during the deadtime but has significantly lower rms value compared to the converter using the finite primary-side parallel inductance to obtain ZVS; 2) has a sharper frequency dependence behavior, suitable for adaptive auxiliary current control using a narrower frequency variation range; 3) works for both the leading and lagging legs with no need for dc capacitors, so the component count is reduced; and 4) uses smaller auxiliary inductors with smaller footprint, fewer number of turns and less proximity effect, lower equivalent series resistance (ESR), and lower conduction losses.

This paper is organized as follows: In Section II, the operation principles of a reference baseline converter and the proposed converter with the auxiliary circuit are explained in detail in steady-state operation. In Section III, the detailed comparison between the proposed and baseline converters is provided. Section IV includes the design process with an example, both for the fixed switching frequency and for the adaptive switching frequency operations. Section V provides the experimental results confirming the analytical predictions.

II. Operation Principle

In this section, first a baseline converter is selected (as a reference design), which uses a finite primary-side parallel inductance, and then the proposed converter is introduced using a resonant auxiliary circuit.

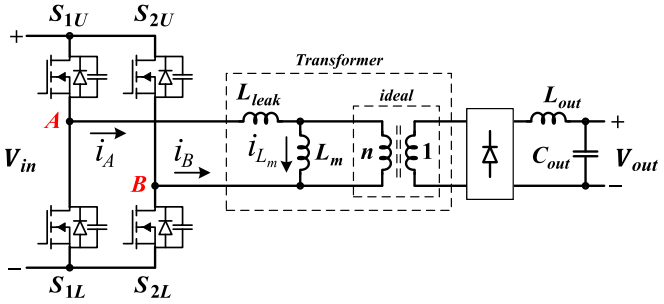

Fig. 2. Full-bridge converter using a transformer with a finite primary-side parallel inductance. Note that L_m can be an external inductor in parallel to the transformer primary terminals.

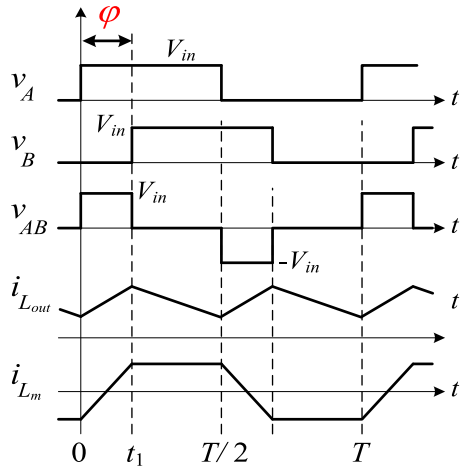

Fig. 3. Main waveforms of the baseline converter of Fig. 2.

A. Assumptions for both the Converters

The following assumptions are considered for the analysis:

1) the converter is in steady-state operation using phase shift modulation;
2) all passive components are ideal with ESR of zero; the small but nonzero resistance of the switches helps settle down to the steady state;
3) the leakage inductance of the transformer, denoted by L_{leak}, is negligible;
4) the duty cycles of the voltages of the full-bridge ac nodes, v_A and v_B, are 50%;
5) the transitions in the voltages of the full-bridge ac nodes are instantaneous

B. Converter Using a Transformer With a Finite Primary-Side Parallel Inductance as the Baseline

The full-bridge converter shown in Fig. 2 is selected as the baseline design and has a relatively inductance in parallel to the transformer primary. Note that it is possible to have a transformer design that its magnetizing inductance acts as L_m. Due to the negligible L_{leak}, the full-bridge voltage v_{AB} appears across L_m and generates i_{L_m} with the direction depicted in Fig. 2.

There are two intervals in each half switching cycle as depicted in Fig. 3. The interbridge phase shift, denoted by φ, is defined as the angle between the rising edges of the leading leg ac voltage (v_A) and that of leading leg (v_B). Following this definition, v_{AB} is represented by

$$v_{AB}(t) = \begin{cases} V_{\text{in}}, & 0 \le t \le t_1 \\ 0, & t_1 \le t \le \frac{T}{2} \end{cases}, v_{AB}(t) = -v_{AB}\left(t - \frac{T}{2}\right) \tag{1}$$

where T is the switching period and $t_1 = (\varphi/\pi)\,T/2$ shown in Fig. 3. Although in Fig. 3 the output inductor current $i_{L_{\text{out}}}$ is considered to be continuous, i.e., in continuous-current mode (CCM), the intervals introduced below are fully determined by the full-bridge voltage and are independent of the continuity of $i_{L_{\text{out}}}$.

1) Interval 1: $0 \le t \le t_1$*:* Interval 1 starts at $t = 0$ when the rising edge of v_A happens and v_{AB} goes from zero to V_{in}. In this interval, the V_{in} appears across L_m and i_{L_m} increases from its initial value $I_{L_m\_0}$

$$i_{L_m}(t) = I_{L_m\_0} + \frac{V_{\text{in}}}{L_m} t. \tag{2}$$

Interval 1 terminates at $t = t_1$ when the rising edge of v_B occurs.

2) Interval 2: $t_1 \le t \le T/2$*:* During this interval, the full-bridge voltage v_{AB} is zero; therefore, i_{L_m} remains constant throughout this interval

$$i_{L_m}(t) = I_{L_m\_0} + \frac{V_{\text{in}}}{L_m} t_1 = I_{L_m\_0} + \frac{V_{\text{in}}}{L_m} \times \left(\frac{\varphi}{\pi}\right) \frac{T}{2}. \tag{3}$$

Interval 2 terminates at $t = T/2$ when the falling edge of v_A happens.

Due to the steady-state operation, $i_{L_m}(t)$ has no dc component and at $t = T/2$ reaches to the negative of its value at $t = 0$, i.e., $\varphi < \pi/2$. Thus

$$I_{L_m\_0} = -\frac{V_{\text{in}} \text{T}}{4L_m} \times \frac{\varphi}{\pi} = -\left(\frac{\pi}{2}\right) \frac{V_{\text{in}}}{L_m \omega_{\text{SW}}} \times \frac{\varphi}{\pi} \tag{4}$$

where ω_{SW} is the switching angular frequency. The voltage v_{AB} of (1) is represented by

$$v_{AB}(t) = \left(\frac{4}{\pi}\right) V_{\text{in}} \sum_{k=1,3,5,\cdots}^{\infty} \frac{1}{k} \sin\left(\frac{k\varphi}{2}\right) \cos\left(k\omega_{\text{SW}} t - \frac{k\varphi}{2}\right). \tag{5}$$

The impedance of L_m is $Z(\omega) = j\omega L_m$; thus, the amplitude of the harmonics of i_{L_m} are determined by

$$I_{L_m\_H_k} = \left(\frac{4}{\pi}\right) V_{\text{in}} \times \frac{1}{k^2 L_m \omega_{\text{SW}}} \sin\left(\frac{k\varphi}{2}\right), k = 1, 3, 5, \ldots \tag{6}$$

Also the rms of i_{L_m}, denoted by $I_{L_m\_\text{rms}}$, is

$$I_{L_m\_\text{rms}} = \left(\frac{\pi}{2}\right) \frac{V_{\text{in}}}{L_m \omega_{\text{SW}}} \left(\frac{\varphi}{\pi}\right) \sqrt{1 - \frac{2\varphi}{3\pi}}. \tag{7}$$

In CCM operation the output inductor peak–peak current ripple is governed by

$$\Delta I_{L_{\rm out}} = \frac{(1-\varphi/\pi)\,\varphi/\pi}{L_{\rm out}\times 2f_{\rm SW}}\times\frac{V_{\rm in}}{n}=\frac{(1-\varphi/\pi)\,\varphi}{L_{\rm out}\omega_{\rm SW}}\times\frac{V_{\rm in}}{n} \quad (8)$$

$$\varphi = \frac{V_{\rm out}+2V_D}{V_{\rm in}/n}\pi \quad (9)$$

with V_D and n being the rectifier diode voltage drop and the transformer turns ratio, respectively. Note that φ is independent of load due to negligible value of $L_{\rm leak}$. Also in CCM the φ value is independent of switching frequency while $\Delta I_{L_{\rm out}}$ is reversely proportional to $\omega_{\rm SW}$. The minimum and maximum of $i_{L_{\rm out}}$ happen at $t=0$ (the rising edge of v_A) and $t=t_1$ (the rising edge of v_B), respectively

$$I_{L_{\rm out}\_\rm min} = I_{L_{\rm out}\_\rm avg} - \frac{1}{2}\Delta I_{L_{\rm out}} \quad (10)$$

$$I_{L_{\rm out}\_\rm max} = I_{L_{\rm out}\_\rm avg} + \frac{1}{2}\Delta I_{L_{\rm out}} \quad (11)$$

where $I_{L_{\rm out}\_\rm avg}$ is determined by the load. As in Fig. 2, the current leaving the ac node of leading leg i_A (lagging leg i_B) satisfies the relation $i_A = i_{L_{\rm out}}/n + i_{L_M}$ ($i_B = -i_{L_{\rm out}}/n - i_{L_M}$). Thus, following the waveforms in Fig. 3, the currents leaving nodes A and B at $t_{v_{\rm A}\nearrow}$ and $t_{v_{\rm B}\nearrow}$, named as $I_{A\_v_{\rm A}\nearrow}$ and $I_{B\_v_{\rm B}\nearrow}$, are

$$\begin{aligned} I_{A\_v_{\rm A}\nearrow} &= i_{L_{\rm out}}(t=0)/n + i_{L_m}(t=0) \\ &= I_{L_{\rm out}\_\rm min}/n + I_{L_m\_0} \end{aligned} \quad (12)$$

$$\begin{aligned} I_{B\_v_{\rm B}\nearrow} &= -i_{L_{\rm out}}(t=t_1)/n - i_{L_m}(t=t_1) \\ &= -I_{L_{\rm out}\_\rm max}/n + I_{L_m\_0}. \end{aligned} \quad (13)$$

In (13), the relation $i_{L_m}(t=t_1) = -I_{L_m\_0}$ is used.

To have ZVS operation in the leading leg at the rising edge of $v_{\rm A}$, the current $I_{A\_v_{\rm A}\nearrow}$ should provide sufficient energy to charge (discharge) the drain–source capacitor of S_{1L} (S_{1U}) during the selected deadtime, t_d. In other words, $I_{A\_v_{\rm A}\nearrow}$ should charge a total effective capacitor denoted by C_{sb} from 0 to $V_{\rm in}$ where C_{sb} is the sum of charge equivalent (and not the energy equivalent) capacitors of S_{1L} and S_{1U} (following [32, p. 247]) plus the stray capacitance of the transformer seen at the primary. To calculate this energy, a common method is to assume that $I_{A\_v_{\rm A}\nearrow}$ remains constants during the deadtime. Using this assumption, the condition for ZVS is

$$I_{A\_v_{\rm A}\nearrow} < \frac{-C_{sb}V_{\rm in}}{t_d}. \quad (14)$$

A more conservative approach is to assume that during the deadtime, the value of i_A changes linearly from $I_{A\_v_{\rm A}\nearrow}$ to zero. Using this second assumption, the condition for ZVS becomes

$$I_{A\_v_{\rm A}\nearrow} < \frac{-2C_{sb}V_{\rm in}}{t_d}. \quad (15)$$

Conditions (14) and (15) can be merged into one

$$I_X = I_{A\_v_{\rm A}\nearrow} + \frac{mC_{sb}V_{\rm in}}{t_d} < 0, m = 1, 2 \quad (16)$$

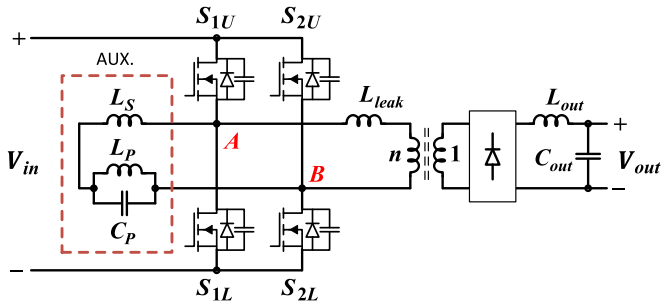

Fig. 4. Proposed full-bridge converter with the resonant auxiliary circuit for both switch legs.

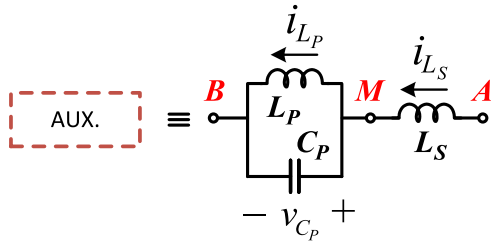

Fig. 5. Major currents and voltages of the resonant auxiliary circuit.

with $m=1$ for (14) and $m=2$ for (15). For any of these approaches, (4) shows that if L_m is selected properly, it is possible to get $I_{A\_v_{\rm A}\nearrow}$ sufficiently negative to generate ZVS. Equation (13) proves that once the ZVS condition for $I_{A\_v_{\rm A}\nearrow}$ is satisfied, $I_{B\_v_{\rm B}\nearrow}$ will be sufficiently negative to maintain ZVS in the lagging leg for any combination of load and input voltage.

C. Proposed Converter using a Resonant Auxiliary Circuit

The proposed converter with the resonant auxiliary circuit is shown in Fig. 4. Compared with the baseline converter, the transformer here has a very large magnetizing inductance such that it draws very small current and is not shown in Fig. 4. There is an auxiliary branch composed of L_S in series with L_PC_P between the ac nodes of the full-bridge. The major voltage and currents of the proposed auxiliary circuit are defined in Fig. 5. Here, one additional assumption is considered: L_S and L_P are similar, with a value of L. The value of C_P is C.

There are three independent state variables for the auxiliary circuit as i_{L_S}, i_{L_P}, and v_C. Following the notations of Fig. 5, the state equations are:

$$\begin{cases} i_{L_S} = i_{L_P} + i_{C_P} \\ v_{C_P} = v_{L_2} \\ v_{AB} = v_{L_S} + v_{C_P} \end{cases} \quad \text{or} \quad \begin{cases} \dfrac{di_{L_S}}{dt} = -\dfrac{1}{L}v_{C_P} + \dfrac{1}{L}v_{AB} \\ \dfrac{di_{L_P}}{dt} = \dfrac{1}{L}v_{C_P} \\ \dfrac{dv_{C_P}}{dt} = \dfrac{1}{C}i_{L_S} - \dfrac{1}{C}i_{L_P} \end{cases}. \quad (17)$$

The initial values of the state variable (at $t=0$) are $I_{0\_L_S}$, $I_{0\_L_P}$, and $V_{0\_C_P}$. Here, we introduce

$$\omega_0 \triangleq \frac{1}{\sqrt{LC/2}}, Z_0 \triangleq \frac{L\omega_0}{\sqrt{2}} = \sqrt{\frac{L}{C}}. \tag{18}$$

Interval 1 ($0 < t < t_1 = (\varphi/\pi)\,T/2$): In this interval $v_{AB}(t) = V_{\text{in}}$ and the state (17) gives

$$\begin{bmatrix} i_{L_S}(t) \\ i_{L_P}(t) \\ v_{C_P}(t) \end{bmatrix} = \begin{bmatrix} \frac{1+\cos\omega_0 t}{2} & \frac{1-\cos\omega_0 t}{2} & -\frac{\sin\omega_0 t}{L\omega_0} \\ \frac{1-\cos\omega_0 t}{2} & \frac{1+\cos\omega_0 t}{2} & \frac{\sin\omega_0 t}{L\omega_0} \\ \frac{1}{C\omega_0}\sin\omega_0 t & -\frac{1}{C\omega_0}\sin\omega_0 t & \cos\omega_0 t \end{bmatrix} \times \begin{bmatrix} I_{0\_L_S} \\ I_{0\_L_P} \\ V_{0\_C_P} \end{bmatrix} + \begin{bmatrix} \sin\omega_0 t + \omega_0 t \\ \omega_0 t - \sin\omega_0 t \\ L\omega_0(1-\cos\omega_0 t) \end{bmatrix} \frac{V_{\text{in}}}{2L\omega_0}. \tag{19}$$

Using $L\omega_0 = Z_0\sqrt{2}$ and $1/C\omega_0 = Z_0/\sqrt{2}$, (19) becomes

$$\begin{bmatrix} Z_0 i_{L_S}(t) \\ Z_0 i_{L_P}(t) \\ v_{C_P}(t) \end{bmatrix} = \frac{1}{2}\begin{bmatrix} 1+\cos\omega_0 t & 1-\cos\omega_0 t & -\sqrt{2}\sin\omega_0 t \\ 1-\cos\omega_0 t & 1+\cos\omega_0 t & \sqrt{2}\sin\omega_0 t \\ \sqrt{2}\sin\omega_0 t & -\sqrt{2}\sin\omega_0 t & 2\cos\omega_0 t \end{bmatrix} \times \begin{bmatrix} I_{0\_L_S} \\ I_{0\_L_P} \\ V_{0\_C_P} \end{bmatrix} + \begin{bmatrix} \sin\omega_0 t + \omega_0 t \\ \omega_0 t - \sin\omega_0 t \\ \sqrt{2}(1-\cos\omega_0 t) \end{bmatrix} \frac{V_{\text{in}}}{2\sqrt{2}}. \tag{20}$$

Interval 1 terminates at $t = t_1 = \varphi T/2\pi$ when the state variables reach to $i_{L_S}(t=t_1) = I_{L_S\_1}$, $i_{L_P}(t=t_1) = I_{L_P\_1}$, and $v_{C_P}(t=t_1) = V_{C_P 1}$, determined by

$$\begin{bmatrix} Z_0 I_{L_S\_1} \\ Z_0 I_{L_P\_1} \\ V_{C_P\_1} \end{bmatrix} = \frac{1}{2}\begin{bmatrix} 1+\cos(2\gamma\varphi) & 1-\cos(2\gamma\varphi) & -\sqrt{2}\sin(2\gamma\varphi) \\ 1-\cos(2\gamma\varphi) & 1+\cos(2\gamma\varphi) & \sqrt{2}\sin(2\gamma\varphi) \\ \sqrt{2}\sin(2\gamma\varphi) & -\sqrt{2}\sin(2\gamma\varphi) & 2\cos(2\gamma\varphi) \end{bmatrix} \times \begin{bmatrix} Z_0 I_{L_S\_0} \\ Z_0 I_{L_P\_0} \\ V_{C_P\_0} \end{bmatrix} + \begin{bmatrix} (2\gamma\varphi)+\sin(2\gamma\varphi) \\ (2\gamma\varphi)-\sin(2\gamma\varphi) \\ \sqrt{2}(1-\cos(2\gamma\varphi)) \end{bmatrix} \frac{V_{\text{in}}}{2\sqrt{2}} \tag{21}$$

where γ is a dimensionless number indicating the ratio of the switching period, $T = 1/f_{\text{SW}}$, to twice of the auxiliary circuit resonance period $T_0 = 1/f_0$.

$$\gamma \triangleq \frac{\omega_0 T}{4\pi} = \frac{\omega_0}{2\omega_{\text{SW}}} = \frac{f_0}{2f_{\text{SW}}} = \frac{T}{2T_0}. \tag{22}$$

Interval 2 ($t_1 < t < T/2$): In this interval, $v_{AB}(t) = 0$ and the state (17) results in

$$\begin{bmatrix} Z_0 i_{L_S}(t) \\ Z_0 i_{L_P}(t) \\ v_{C_P}(t) \end{bmatrix} = \frac{1}{2} \begin{bmatrix} 1+\cos\omega_0 t' & 1-\cos\omega_0 t' & -\sqrt{2}\sin\omega_0 t' \\ 1-\cos\omega_0 t' & 1+\cos\omega_0 t' & \sqrt{2}\sin\omega_0 t' \\ \sqrt{2}\sin\omega_0 t' & -\sqrt{2}\sin\omega_0 t' & 2\cos\omega_0 t' \end{bmatrix} \begin{bmatrix} I_{1\_L_S} \\ I_{1\_L_P} \\ V_{1\_C_P} \end{bmatrix} \tag{23}$$

where $t' = t - (\varphi/\pi)\,T/2$. At $t = T/2$, we have $\omega_0 t' = \omega_0(1-\varphi/\pi)\,T/2 = 2\gamma(\pi-\varphi)$ and

$$\begin{bmatrix} Z_0 I_{L_S\_2} \\ Z_0 I_{L_P\_2} \\ V_{C_P\_2} \end{bmatrix} = \frac{1}{2} \begin{bmatrix} 1+\cos(2\gamma(\pi-\varphi)) & 1-\cos(2\gamma(\pi-\varphi)) & -\sqrt{2}\sin(2\gamma(\pi-\varphi)) \\ 1-\cos(2\gamma(\pi-\varphi)) & 1+\cos(2\gamma(\pi-\varphi)) & \sqrt{2}\sin(2\gamma(\pi-\varphi)) \\ \sqrt{2}\sin(2\gamma(\pi-\varphi)) & -\sqrt{2}\sin(2\gamma(\pi-\varphi)) & 2\cos(2\gamma(\pi-\varphi)) \end{bmatrix} \times \begin{bmatrix} Z_0 I_{L_S\_1} \\ Z_0 I_{L_P\_1} \\ V_{C_P\_1} \end{bmatrix} \tag{24}$$

with $\varphi' = \pi - \varphi$. At steady-state operation, the state variables of i_{L_S}, i_{L_P}, and v_C have no dc component. Also, for all three of them $I_{L_S\_2} = -I_{L_S\_0}$, $I_{L_P\_2} = -I_{L_P\_0}$, and $V_{C_P\_2} = -V_{C_P\_0}$.

From (21) and (24)

$$\begin{bmatrix} 3+\cos(2\pi\gamma) & 1-\cos(2\pi\gamma) & -\sqrt{2}\sin(2\pi\gamma) \\ 1-\cos(2\pi\gamma) & 3+\cos(2\pi\gamma) & \sqrt{2}\sin(2\pi\gamma) \\ \sqrt{2}\sin(2\pi\gamma) & -\sqrt{2}\sin(2\pi\gamma) & 2+2\cos(2\pi\gamma) \end{bmatrix} \begin{bmatrix} Z_0 I_{L_S\_1} \\ Z_0 I_{L_P\_1} \\ V_{C_P\_1} \end{bmatrix} = \begin{bmatrix} (2\gamma\varphi)+\sin(2\gamma\varphi) \\ (2\gamma\varphi)-\sin(2\gamma\varphi) \\ \sqrt{2}(1-\cos(2\gamma\varphi)) \end{bmatrix} \frac{V_{\text{in}}}{\sqrt{2}}. \tag{25}$$

The condition for (25) to have unique answers is

$$\det \begin{bmatrix} 3+\cos(2\pi\gamma) & 1-\cos(2\pi\gamma) & -\sqrt{2}\sin(2\pi\gamma) \\ 1-\cos(2\pi\gamma) & 3+\cos(2\pi\gamma) & \sqrt{2}\sin(2\pi\gamma) \\ \sqrt{2}\sin(2\pi\gamma) & -\sqrt{2}\sin(2\pi\gamma) & 2+2\cos(2\pi\gamma) \end{bmatrix} \neq 0 \tag{26}$$

or

$$\cos(2\pi\gamma) \neq -1 \quad \text{or} \quad \gamma \neq n - 1/2, n \in N. \tag{27}$$

This is equivalent with $\omega_{\text{SW}} \neq \omega_0/(2n-1)\; n \in N$. To satisfy this condition it is necessary to ensure that ω_{SW} varies within a range of frequencies that neither ω_{SW} nor any of its odd harmonics are close to ω_0. To emphasize it further, we examine the net impedance between node A and node B in Fig. 5

$$Z(\omega) = j\omega L\left[\frac{2-LC\omega^2}{1-LC\omega^2}\right] = j2\omega L\left[\frac{1-\omega^2/\omega_0^2}{1-\omega^2/\left(\omega_0/\sqrt{2}\right)^2}\right]. \tag{28}$$

Equation (28) reveals that the forbidden γ values in (27) belong to the situations in which ω_{SW} or one of its odd harmonics is a zero of $Z(\omega)$

$$I_{1\_L_S} = \left[\gamma\frac{\varphi}{\pi} + \frac{\sin(\gamma\varphi)\cos(\gamma(\pi-\varphi))}{\pi\cos(\gamma\pi)}\right] I_{\text{base}} \tag{29}$$

$$I_{1\_L_P} = \left[\gamma\frac{\varphi}{\pi} - \frac{\sin(\gamma\varphi)\cos(\gamma(\pi-\varphi))}{\pi\cos(\gamma\pi)}\right] I_{\text{base}} \tag{30}$$

$$V_{1\_C_P} = -\frac{\sin(\gamma\varphi)\sin(\gamma(\pi-\varphi))}{2\cos(\gamma\pi)}V_{in} \tag{31}$$

where

$$I_{\text{base}} \triangleq \left(\frac{\pi}{2}\right)\frac{V_{\text{in}}}{L\omega_0}. \tag{32}$$

From (24)

$$I_{L_S\_0} = -I_{L_S\_1}, \quad I_{L_P\_0} = -I_{L_P\_1}, \text{ and } V_{C_P\_0} = V_{C_P\_1} \tag{33}$$

The second half period is obtainable by symmetry. Using (33) in conjunction with (29) to (31), it is possible to represent $I_{L_S\_0}$, $I_{L_P\_1}$, and $V_{C_P\_0}$ by introducing per-unit quantities as

$$I_{L_S\_0} = I_{L_S\_0\_\text{PU}} \times I_{\text{base}}$$

$$I_{L_S\_0\_\text{PU}} = -\left[\gamma\frac{\varphi}{\pi} + \frac{\sin(\gamma\varphi)\cos(\gamma(\pi-\varphi))}{\pi\cos(\gamma\pi)}\right] \tag{34}$$

$$I_{L_P\_0} = I_{L_P\_0\_\text{PU}} \times I_{\text{base}}$$

$$I_{L_P\_0\_\text{PU}} = -\left[\gamma\frac{\varphi}{\pi} - \frac{\sin(\gamma\varphi)\cos(\gamma(\pi-\varphi))}{\pi\cos(\gamma\pi)}\right] \tag{35}$$

$$V_{C_P\_0} = V_{C_P\_0\_\text{PU}} \times V_{\text{in}}$$

$$V_{C_P\_0\_\text{PU}} = -\frac{\sin(\gamma\varphi)\sin(\gamma(\pi-\varphi))}{2\cos(\gamma\pi)}. \tag{36}$$

The typical waveforms of v_M, i_{L_S}, i_{L_P}, and v_{C_P} for the case of $\gamma = 1$ are illustrated in Fig. 6(a)–(d) for $\varphi < \pi/2$, $\varphi = \pi/2$ $\varphi > \pi/2$, and $\varphi = \pi$, respectively.

The impedance of the auxiliary seen from node M to the ground is given by $Z(\omega)$ in (28); thus, the amplitude of the harmonics of i_{L_S} are determined by

$$I_{L_S\_H_k} = \left(\frac{4}{\pi}\right)\frac{2\gamma}{k^2}\frac{V_{\text{in}}}{\omega_0 L}\left[\frac{2\gamma^2-k^2}{4\gamma^2-k^2}\right]\sin\left(\frac{k\varphi}{2}\right). \tag{37}$$

And using (32)

$$I_{L_S\_H_k} = I_{L_S\_H_k\_\text{PU}} \times I_{\text{base}}$$

$$I_{L_S\_H_k\_\text{PU}} = \left(\frac{4}{\pi}\right)^2\frac{\gamma}{k^2}\left[\frac{2\gamma^2-k^2}{4\gamma^2-k^2}\right]\sin\left(\frac{k\varphi}{2}\right). \tag{38}$$

Substituting $\varphi = \pi$ in (38) leads to (28) in [28] (with $\gamma = 1/2r$). As in the case of previous section, we have the relation $i_A = i_{L_{\text{out}}}/n + i_{L_S}$ ($i_B = -i_{L_{\text{out}}}/n - i_{L_S}$). Thus, $I_{A\_v_A\nearrow}$ and $I_{B\_v_B\nearrow}$ are

$$I_{A\_v_A\nearrow} = i_{L_{\text{out}}}(t=0)/n + i_{L_S}(t=0)$$

$$= I_{L_{\text{out}}\_\min}/n + I_{L_S\_0} \tag{39}$$

$$I_{B\_v_B\nearrow} = -i_{L_{\text{out}}}(t=t_1)/n - i_{L_S}(t=t_1)$$

$$= -I_{L_{\text{out}}\_\max}/n + I_{L_S\_0} \tag{40}$$

with $I_{L_S\_0}$ from (29) and (33).

Similar to the case of the baseline converter, following any of these approaches in (14) or (15) (34) shows the possibility of designing the resonant auxiliary to have $I_{A\_v_A\nearrow}$ sufficiently negative and maintaining ZVS for the leading leg. (40) also confirms that having the ZVS condition for $I_{A\_v_A\nearrow}$ is a sufficient condition to get $I_{B\_v_B\nearrow}$ negative enough to maintain ZVS in the lagging leg for any combination of load and input voltage.

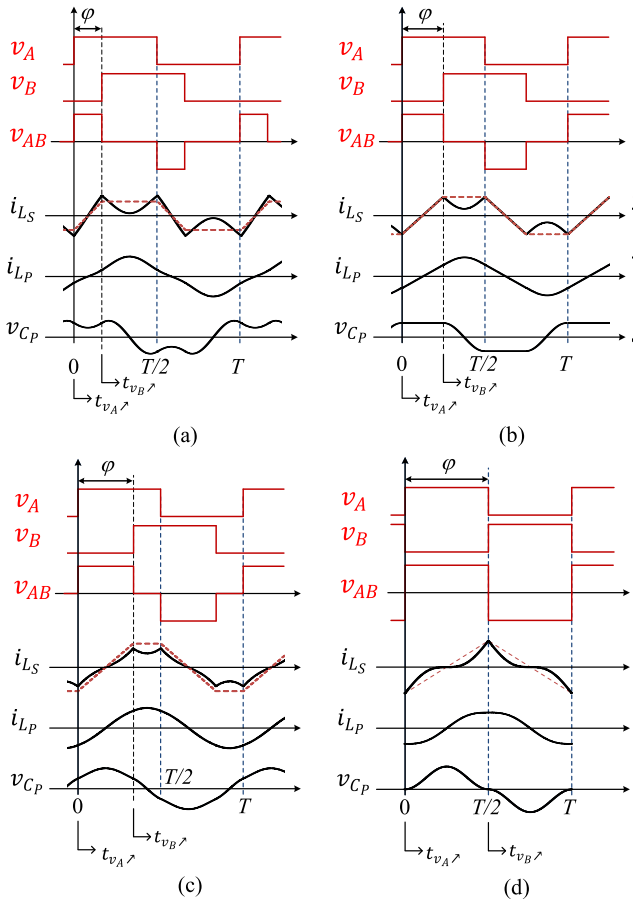

Fig. 6. Auxiliary major voltage and current waveforms for $\gamma = 1$: (a) $\varphi < \pi/2$, (b) $\varphi = \pi/2$, (c) $\varphi > \pi/2$, and (d) $\varphi = \pi$. The dotted lines belong to the baseline converter.

III. Comparison of Baseline and Resonant Auxiliary Circuits

To have an objective comparison between the baseline and the proposed converters it is required to select a matching condition and choose the components in two circuits for a similar performance (as far as ZVS operation is concerned) at the matched condition. Here, the matching is selected to be at $\varphi = \pi$ and $\omega_{\text{SW}} = \omega_0/2$ (or $\gamma = 1$ for the resonant auxiliary circuit). The components are selected such that at this condition both i_{L_m} in the baseline converter and i_{L_S} in the proposed converter have similar peak value. For the baseline converter substituting $\varphi = \pi$ in (4) leads to

$$I_{L_m\_0} = -\left(\frac{\pi}{2}\right)\frac{V_{\text{in}}}{L_m\omega_{\text{SW}}}. \tag{41}$$

And for the resonant auxiliary, inserting $\gamma = 1$ and $\varphi = \pi$ in (33) results in

$$I_{L_S\_0} = -I_{\text{base}} = -\left(\frac{\pi}{2}\right)\frac{V_{\text{in}}}{L\omega_0} = -\left(\frac{\pi}{2}\right)\frac{V_{\text{in}}}{2L\omega_{\text{SW}}}. \tag{42}$$

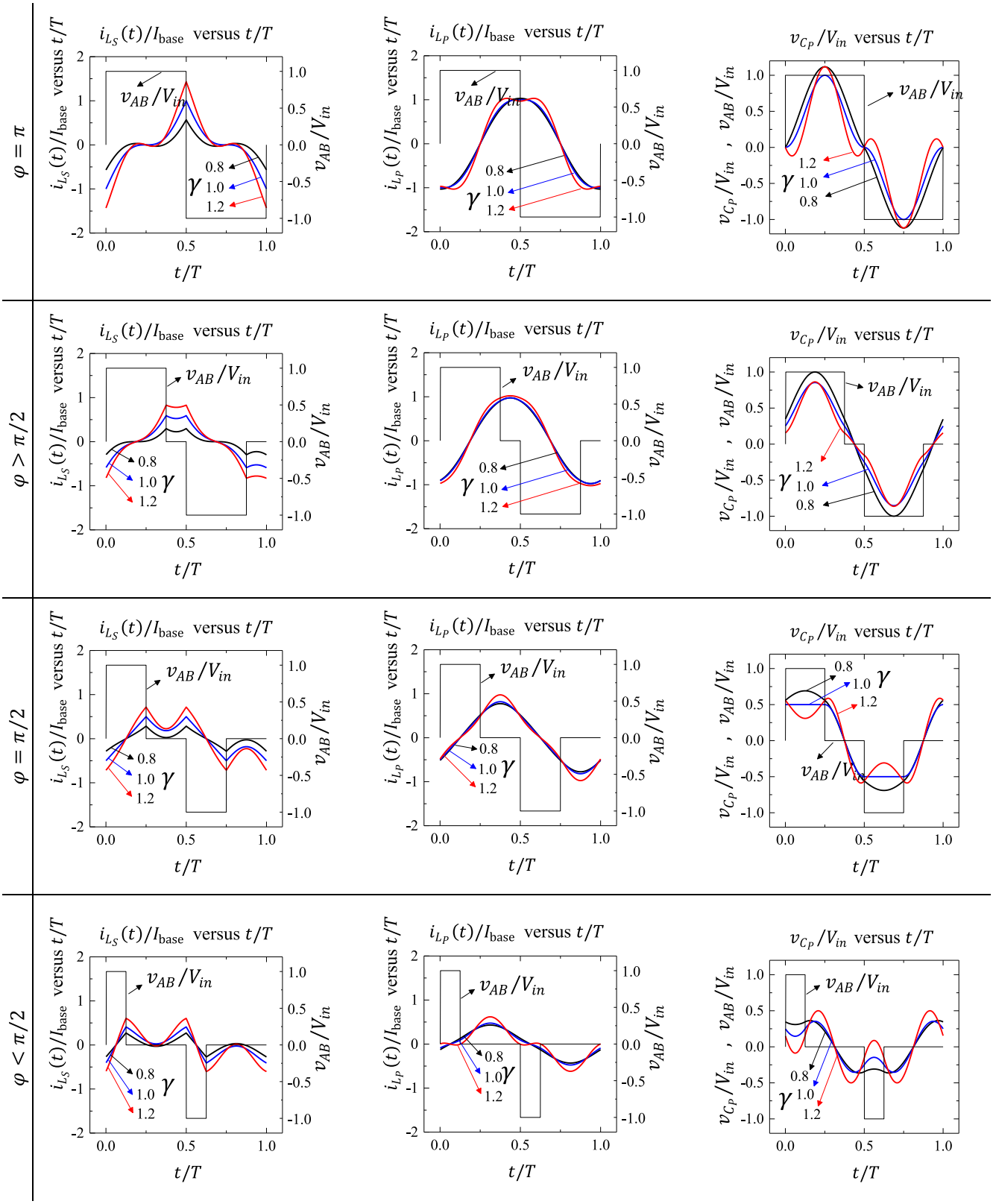

Fig. 7. $i_{L_s}(t)/I_{\text{base}}$ (left), $i_{L_p}(t)/I_{\text{base}}$ (middle), and $\nu_{c_P}(t)/V_{\text{in}}$ versus t/T for $\gamma = 0.8$, 1, and 1.2. The rows belong to $\varphi = \pi$, $\varphi > \pi/2$, $\varphi = \pi/2$ $\varphi < \pi/2$, and $\varphi < \pi/2$, respectively.

Equal peak currents for both auxiliaries require

$$L_m = 2L \tag{43}$$

and C is found from (18). To simplify the visualization of graphs in this section, the definitions of γ in (22) and I_{base} in (32) are extended to the baseline converter as well. Equation (4) for the baseline converter is rewritten by introducing per-unit quantity $I_{L_m\_0\_\text{PU}}$ as

$$I_{L_m\_0} = I_{L_m\_0\_\text{PU}} \times I_{\text{base}}, \quad I_{L_m\_0\_\text{PU}} = -\gamma\frac{\varphi}{\pi}. \tag{44}$$

And (6) becomes

$$\begin{aligned} I_{L_m\_H_k} &= I_{L_m\_H_k\text{PU}} \times I_{\text{base}} \\ I_{L_m\_H_k\_\text{PU}} &= \left(\frac{4}{\pi}\right)^2 \frac{\gamma}{2k^2} \sin\left(\frac{k\varphi}{2}\right). \end{aligned} \tag{45}$$

Substituting $\varphi = \pi$ in (45) leads to (26) in [28]. The same process for (7) results in

$$\begin{aligned} I_{L_m\_\text{rms}} &= I_{L_m\_\text{rms\_PU}} \times I_{\text{base}} \\ I_{L_m\_\text{rms\_PU}} &= \gamma\frac{\varphi}{\pi}\sqrt{1-\frac{2\varphi}{3\pi}}. \end{aligned} \tag{46}$$

The presence of parameter γ and its influence on the behavior of i_{L_S}, i_{L_P}, and v_{C_P} is the major difference between the baseline converter and the proposed one. In Fig. 6, the dashed lines show the waveform of $i_{L_m}(t)$ alongside of $i_{L_S}(t)$ for $\gamma = 1$. In Fig. 6(d), phase shift φ is equal to π and $I_{L_m\_0} = I_{L_S\_0}$ compatible with the selection in (43). It is evident that the resonant auxiliary circuit has a lower rms current with the same peak value. Fig. 6(a) belongs to the case of $0 < \varphi < \pi/2$ where $I_{L_S\_0}$ is greater than $I_{L_m\_0}$. In Fig. 6(b), φ is $\pi/2$ and $I_{L_S\_0}$ and $I_{L_m\_0}$ are equal. And with $\pi/2 < \varphi < \pi$, shown in Fig. 6(c), $I_{L_S\_0}$ is slightly than $I_{L_m\_0}$.

The per-unit waveforms of v_M, i_{L_S}, i_{L_P}, and v_{C_P} for three choices of $\gamma = 0.8$, 1, and 1.2 are illustrated in Fig. 7(a)–(d) for $\varphi < \pi/2$, $\varphi = \pi/2$, $\varphi > \pi/2$, and $\varphi = \pi$, respectively. For any choice of φ increasing γ means longer switching period. The rate of growth in $|I_{L_S\_0}|$ in time is faster than linear similar growth observed in $|I_{L_m\_0}|$; therefore, with smaller variation in switching frequency, it possible to adjust the peak current in the proposed auxiliary. The peak current adjustability with reduced frequency range allows adaptively tuning of the auxiliary current to the level required for ZVS but not beyond necessary (that will negatively impact the overall converter efficiency).

Fig. 8 illustrates the variation of $|I_{L_m\_0\text{PU}}|$ versus phase shift for $0.8 \le \gamma \le 1.2$. As expected from (44), the behavior is linear with both φ and γ. It is evident that $\pm 20\%$ variation in γ [i.e., $\pm 20\%$ variation in the switching period T as in (22)] results in $\pm 20\%$ variation in $|I_{L_m\_0\text{PU}}|$. This means that, for example, to have half the $I_{L_m\_0\text{PU}}$ at any specific φ, γ should become half or the switching frequency should be doubled, which is not desirable.

Fig. 9 depicts the variation of $|I_{L_S\_0\_\text{PU}}|$ versus phase shift for the same range of γ as in Fig. 8 for the resonant auxiliary. Comparing Figs. 8 and 9 reveals that the resonant auxiliary provides larger peak current variation versus γ so it is possible to adjust the current needed for the ZVS with a smaller frequency variation. To do so we need to ensure that varying the frequency does not result is extra current/voltage stress in/across any components. Fig. 10 confirms that the current in L_P does not change much versus the frequency change and the maximum $I_{L_P\_0\_\text{PU}}$ remains about 1. Fig. 11 also assures that the voltage across C_P does not increase considerably and that $|V_{C_P\_0\_\text{PU}}|$ does not

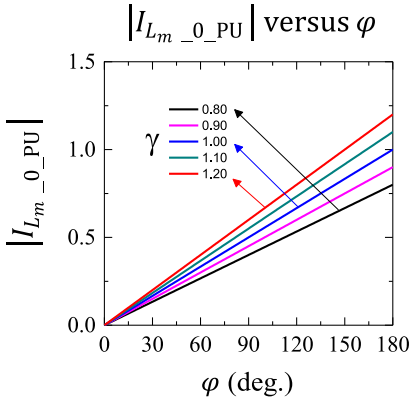

Fig. 8. $|I_{L_m\_0\_\text{PU}}|$ versus φ for $0.8 \le \gamma \le 1.2$.

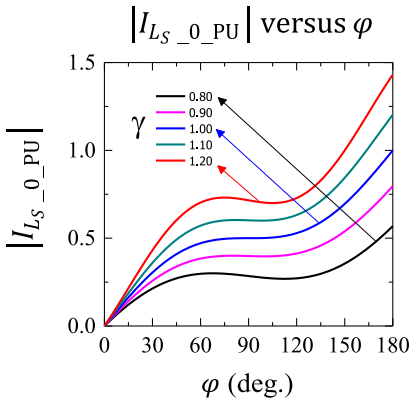

Fig. 9. $|I_{L_S\_0\_\text{PU}}|$ versus φ for $0.8 \le \gamma \le 1.2$.

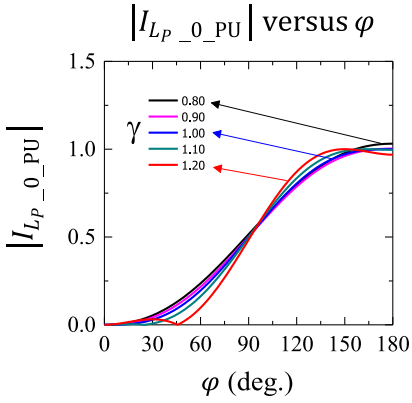

Fig. 10. $|I_{L_P\_0\_\text{PU}}|$ versus φ for $0.8 \le \gamma \le 1.2$.

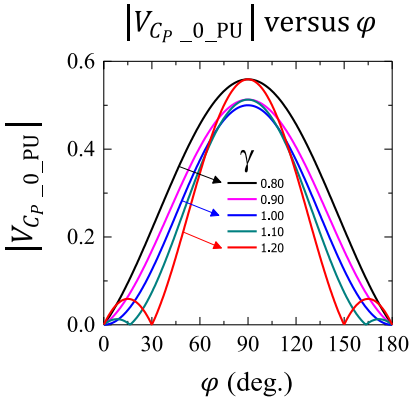

Fig. 11. $|V_{C_P\_0\_PU}|$ versus γ for $0.8 \leq \gamma \leq 1.2$.

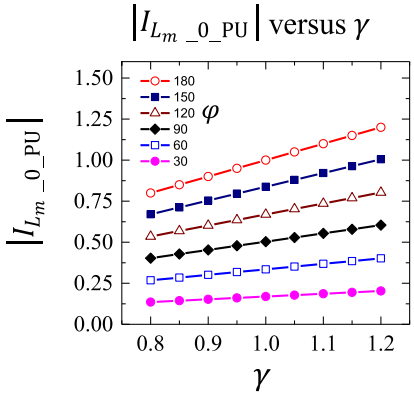

Fig. 12. $|I_{L_m\_0\_PU}|$ versus γ for $30^\circ \leq \varphi \leq 180^\circ$.

exceed 0.6. Therefore, there is no need to select a bulky and expensive capacitor for the resonant auxiliary circuit.

Figs. 12 and 13 depict the variations of $|I_{L_m\_0\_PU}|$ and $|I_{L_S\_0\_PU}|$ versus $0.8 \leq \gamma \leq 1.2$ for a variety of phase shifts. Two major differences are noticeable: first, for any φ value, the rate of change versus γ is higher for $|I_{L_S\_0\_PU}|$ compared to $|I_{L_m\_0\_PU}|$ as expected. Second, for the range of $60^\circ \leq \varphi \leq 120^\circ$ (which is the case for the majority of the operational time), this rate is almost constant for $|I_{L_S\_0\_PU}|$ in contrary to $|I_{L_m\_0\_PU}|$. This constant rate simplifies the design of control for adaptive switching frequency selection detailed in [27] and [28] (to adjust the auxiliary peak current).

Fig. 14 shows the difference between the rms currents in L_m of baseline converter $I_{L_m\_\mathrm{rms}}$ and in L_S $I_{L_S\,\mathrm{rms}}$ calculated numerically for a similar peak current for three choices of $\gamma = 0.8$, 1, and 1.2. For any peak current value at any γ, the resonant auxiliary has at least 20% lower rms current. This reduces the conduction losses with no impact on the ZVS functionality.

IV. Design Example

In this section, the design steps of the proposed converter are given. The converter specifications are given in Table I.

First, the transformer turn ratio n is selected. For the lowest $V_{\mathrm{in}} = 200$ V and nominal $V_{\mathrm{out}} = 57.6$ V, we reserve 40° for the current sensor demagnetization and less than 10° to compensate of the voltage drops across real elements. From (9) with $\varphi = 130^\circ$ and $V_D = 0.7$ V, the value of $n = 2.45$ is obtained. So we select n to be equal to 2.5. Substituting $n = 2.5$ for $V_{\mathrm{in}} = 200$ V back into (9)

$$\varphi_{200\mathrm{V}} = \frac{57.6 + 2 \times 0.7}{200/2.5} \times \pi = 2.317 \text{ rad} = 132.8^\circ \quad (47)$$

which is compatible with the reserved angle for the current sensor demagnetization and voltage drops. Fig. 15 shows the variations of φ to regulate V_{out} at 57.6 V for the range of V_{in} listed in Table I. As mentioned before, in CCM, φ is independent of switching frequency.

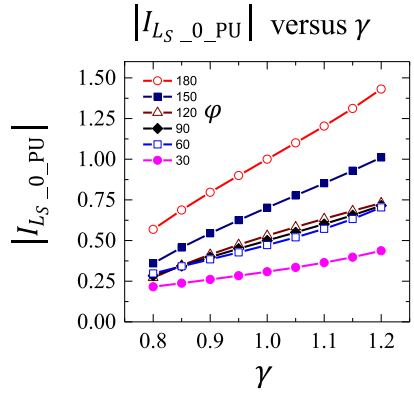

Fig. 13. $|I_{L_S\_0\_PU}|$ versus γ for $30^\circ \leq \varphi \leq 180^\circ$.

A. Converter Operating at Fixed Switching Frequency

The nominal load current is $I_{L_{\mathrm{out}}_\mathrm{avg}} = 750/57.6 = 13$A. The criterion considered here for selecting output filter L_{out} is to guarantee the converter operation in CCM for the loads above 20% (i.e., $I_{L_{\mathrm{out}}\_\mathrm{avg}} > 2.6$ A) for the entire input voltage range. Equation (8) shows that the $\Delta I_{L_{\mathrm{out}}}$ increases with V_{in} when φ is adjusted to maintain output voltage regulation (shown in Fig. 15). At the boundary of CCM and discontinuous current mode (DCM), $I_{L_{\mathrm{out}}\_\mathrm{min}}$ reaches to zero; thus, from (10)

$$\Delta I_{L_{\mathrm{out}}\_\mathrm{boundary}} = 2 I_{L_{\mathrm{out}}\_\mathrm{avg}}. \quad (48)$$

For the boundary to happen at $I_{L_{\mathrm{out}}\_\mathrm{avg}} = 2.6$ A, we get $\Delta I_{L_{\mathrm{out}}\_\mathrm{boundary}} = 5.2$ A. C_{out} is calculated to have less than 50 mV of peak–peak voltage ripple when passing the highest peak–peak ripple current of 5.2 A, and thus, C_{out} is selected to be 250 μF.

The largest $\Delta I_{L_{\mathrm{out}}}$ happens at the maximum of $V_{\mathrm{in}} = 300$ V. Thus, from (9)

$$\varphi_{300\mathrm{V}} = \frac{57.6 + 2 \times 0.7}{300/2.5} \times \pi = 1.545 \,\mathrm{rad} = 88.5^\circ. \quad (49)$$

By substituting $\varphi_{300\,\mathrm{V}} = 88.5^\circ$, $\Delta I_{L_{\mathrm{out}}\_\mathrm{boundary}} = 5.2$ A, $n = 2.5$, and constant switching frequency of $f_{\mathrm{SW}} = 200$ kHz in (8), L_{out} is calculated as 14.39 μH, and we select it to be

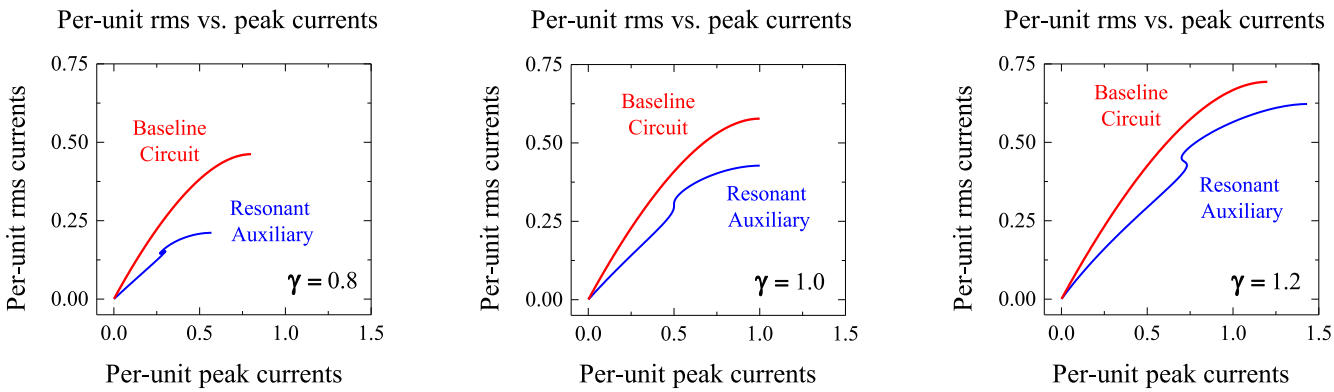

Fig. 14. Per-unit rms versus peak currents in L_m of baseline converter and L_S of resonant auxiliary for $\gamma = 0.8$, 1, and 1.2.

TABLE I
CONVERTER SPECIFICATIONS

Parameter	Value
Nominal output power	750 W
Input voltage	200–300 V
Nominal output voltage	57.6 V
Switching frequency	≥200 kHz

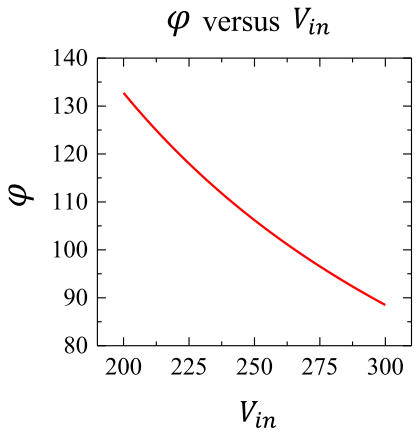

Fig. 15. Variations of φ to regulate $V_{\rm out}$ at 57.6 V for 200 V $\leq V_{\rm in} \leq$ 300 V.

15 μH. Fig. 16 illustrates variations of $\Delta I_{L_{\rm out}}$ versus $V_{\rm in}$ in CCM, from (8) for $L_{\rm out} = 15\,\mu$H.

To guarantee the ZVS condition in (16), $I_{A\_v_{\rm A}\nearrow}$ should be calculated from (39), so knowing $I_{L_{\rm out}\_\min}/n$ is required. Fig. 17 shows the variation of $I_{L_{\rm out}\_\min}/n$ versus $V_{\rm in}$ in full load obtained from (10) using $f_{\rm SW} = 200\,$kHz and $L_{\rm out} = 15\,\mu$H .

Using (32) and (34), the quantity I_X in (16) can be written as

$$I_X = \frac{1}{n}\left[I_{L_{\rm out\_avg}} - \frac{1}{2}\frac{(1-\varphi/\pi)\,\varphi}{L_{\rm out}\omega_{\rm SW}} \times \frac{V_{\rm in}}{n}\right] - \left[\gamma\frac{\varphi}{\pi} + \frac{\sin(\gamma\varphi)\cos(\gamma(\pi-\varphi))}{\pi\cos(\gamma\pi)}\right] \times \left(\frac{\pi}{2}\right)\frac{V_{\rm in}}{L\omega_0} + \frac{mC_{sb}V_{\rm in}}{t_d} \quad (50)$$

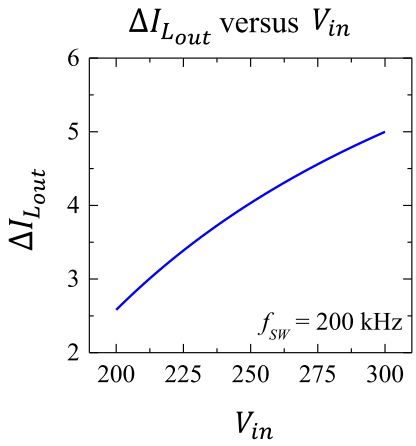

Fig. 16. Variations $\Delta I_{L_{\rm out}}$ in CCM for 200 V $\leq V_{\rm in} \leq$ 300 V at $f_{\rm SW} =$ 200 kHz when φ is varied as in Fig. 15.

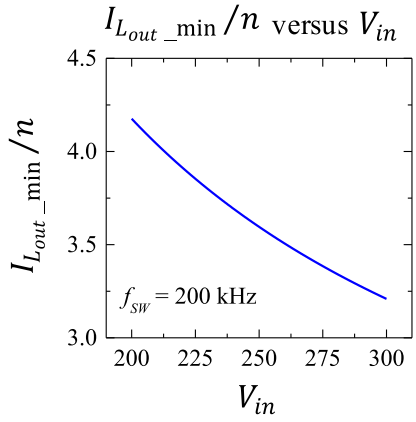

Fig. 17. Variation of $I_{L_{\rm out}\_\min}/n$ for 200 V $\leq V_{\rm in} \leq$ 300 V at $f_{\rm SW} =$ 200 kHz and full load in CCM.

with φ from (8) adjusted to maintain output voltage regulation (see Fig. 15). Assuming that constant frequency γ is fixed and by selecting $\gamma = 1$, from (22), we get $\omega_0 = 2.51$ Mrad/s. Assuming $C_{sb} = 1$ nF, $t_d = 200$ ns, and $I_{L_{\rm out\_avg}} = 13$ A, the only unknown in (50) is L (the value of L_S and L_P, which are assumed to be identical) for the parameter m.

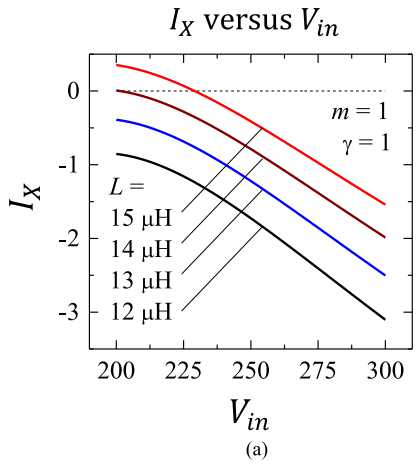

(a)

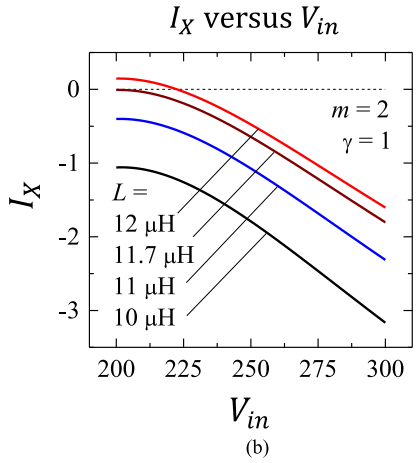

(b)

Fig. 18. Variation of I_X in (50) for 200 V $\leq V_{\rm in} \leq$ 300 V at $f_{\rm SW} =$ 200 kHz and $\gamma = 1$ for (a) $m = 1$ and (b) $m = 2$.

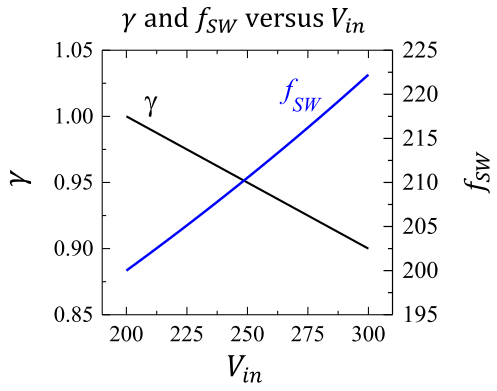

Fig. 19. Selected γ as a function of $V_{\rm in}$ and variation of $f_{\rm SW}$ (in kHz) for 200 V $\leq V_{\rm in} \leq$ 300 V.

Fig. 18 shows the variation of I_X In (50) for 200 V $\leq V_{\rm in} \leq$ 300 V at $f_{\rm SW} =$ 200 kHz and $\gamma = 1$ for two choices of $m = 1$ and 2, it is evident that the selection of L value for the resonant auxiliary should be done for the point $V_{\rm in} = 200$ V due to the decreasing behavior of I_X with $V_{\rm in}$. Depending on the assumed m for the design, a value between 11.7 and 14 μH can be selected for L. Knowing ω_0, we can find C from (18).

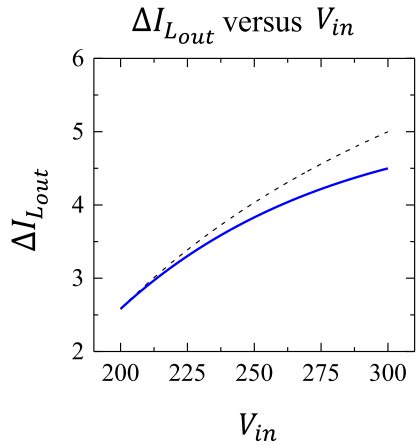

Fig. 20. Variations $\Delta I_{L_{\rm out}}$ in CCM for frequency variation of Fig. 19. The dashed line belong to Fig. 16.

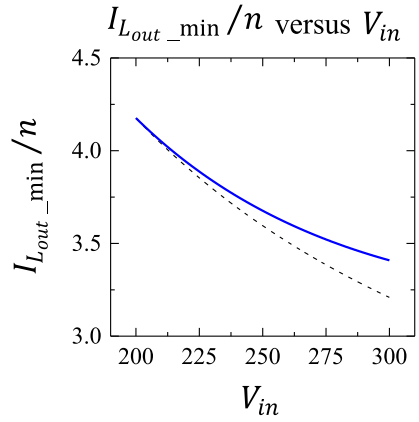

Fig. 21. Variation of $I_{L_{\rm out}\_\rm min}/n$ for frequency variation of Fig. 19 and full load in CCM. The dashed line belong to Fig. 17.

B. Converter Operating with Adaptive Switching Frequency

It was shown that ZVS operation requires the condition in (16) be satisfied; however, highly negative also not desirable due to incurring unnecessary conduction losses. It is possible to keep I_X negative but close to zero for all $V_{\rm in}$ values using adaptive switching frequency selection. Here, we select the following scheme:

$$\gamma\left(V_{\rm in}\right) = 1 - \frac{\overline{V_{\rm in}}}{300} \times 0.1 \text{ or}$$

$$f_{\rm SW}\left(V_{\rm in}\right) = \frac{\omega_0/2\pi}{2\left(1 - (\overline{V_{\rm in}}/300) \times 0.1\right)}. \tag{51}$$

Here, $\overline{V_{\rm in}}$ is the moving average of $V_{\rm in}$ and $f_{\rm SW}$ is found from (22) as shown in Fig. 19. The averaging happens very slowly, in the range of seconds, so the converter is essentially always at the steady state and the rapid changes in $V_{\rm in}$ are not seen by the adaptive controller due to the averaging scheme. By reusing $\omega_0 = 2.51$ Mrad/s from the previous section, $f_{\rm SW}$ varies from 200 to 222 kHz, i.e., less than 12% variation, which does not generate excessive pressure on the gate drivers and does not result in difficulties for EMI filter design.

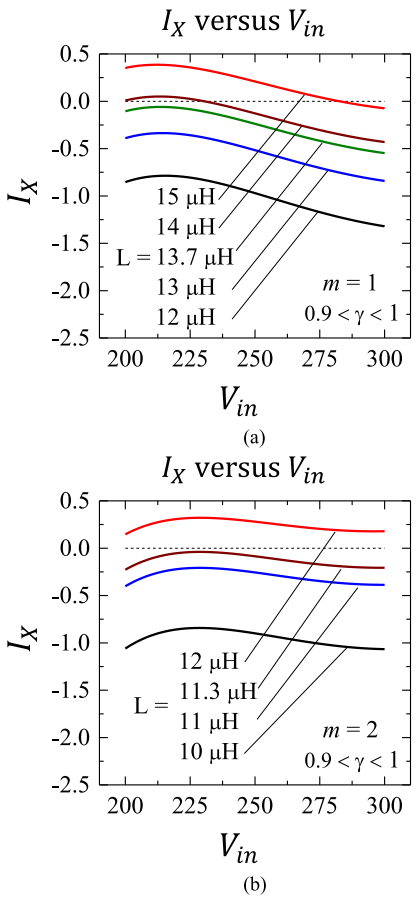

Fig. 22. Variation of I_X in (50) for 200 V $\leq V_{\text{in}} \leq$ 300 V with variable ω_{SW} of (51) for (a) $m = 1$ and (b) $m = 2$.

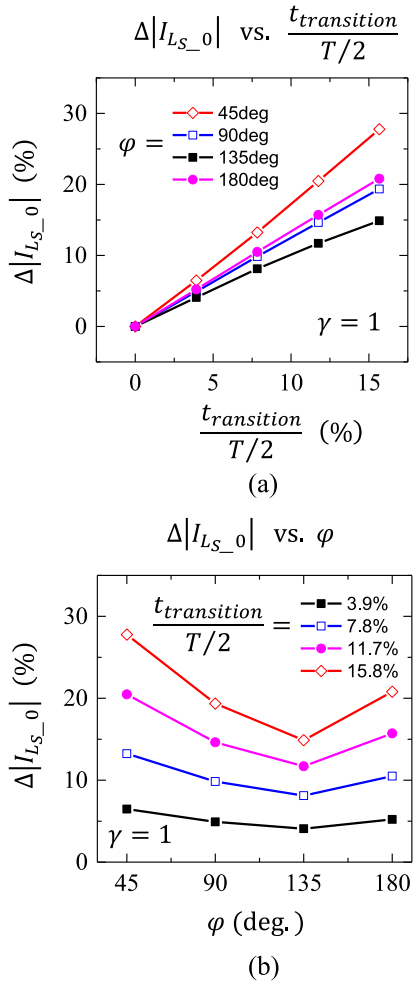

Fig. 23. Variations of $\Delta\left|I_{Ls\,0}\right|$ versus (a) $t_{\text{transition}}/(T/2)$ and (b) φ.

Fig. 20 shows the variations of $\Delta I_{L_{\text{out}}}$ versus V_{in} in CCM for $L_{\text{out}} = 15\ \mu$H with adaptive f_{SW} of (51) considered in (8). Compared to Fig. 16 the variation of $\Delta I_{L_{\text{out}}}$ versus V_{in} are less, due to the higher switching frequency at higher input voltages. Subsequently, Fig. 21 shows that the drop in $I_{L_{\text{out}}\_\min}/n$ at higher V_{in} is less than what we had in Fig. 16. Therefore, the available auxiliary current is better utilized to compensate higher $I_{L_{\text{out}}\_\min}/n$ values toward ensuring ZVS operation.

Fig. 22 shows the variation of I_X versus V_{in} with variable f_{SW} of (51) for $m = 1$ and 2. This time the entire range of V_{in} should be considered for correct selection of L. Depending on the assumed m for the design, a value between 11.3 to 13.7 μH can be selected for L. Again, C can be found from (18) knowing ω_0.

C. Effect of Noninstantaneous Voltage Transitions

In Section II-A, we assumed that the transitions in the full-bridge ac-node voltages are instantaneous. In reality, the transition is not instantaneous and takes a certain nonzero time. The duration of this time depends on the load condition, i.e., for a similar peak auxiliary current the transition takes longer at heavy loads because a greater portion of the auxiliary current is taken to compensate the load current reflected to the primary side of the transformer. Here the longest transition time is denoted by $t_{\text{transition}}$. It is important to note that in presence of a complete ZVS operation, the transition gets completed before the end of the deadtime (of the gate signals), so the next switch can turn on under zero voltage. In other words, $t_{\text{transition}} < t_d$.

With an instantaneous voltage transition studying I_{Ls_0} of (34) is sufficient to design the auxiliary. When the voltage transitions are noninstantaneous, the average of the auxiliary current during $t_{\text{transition}}$ interval should be considered instead of I_{Ls_0}.

TABLE II
CONVERTER COMPONENT VALUES

Component	Value
Switches	STW69N65M5
Main transformer	ETD44, 3F3, 2.5:1 Leakage Inductance (Primary) < 500 nH Magnetizing Inductance (Primary) > 5mH
Rectifier diodes	STPS30100ST
Output inductor	RM10, 3F3 10 t, gap: 1 mm, 15 μH
Output capacitor	250 μF, 100 V
Auxiliary inductors	RM10, 3F3 9 t, gap: 1 mm, 11 μH
Auxiliary capacitor	30 nF, 1000 V

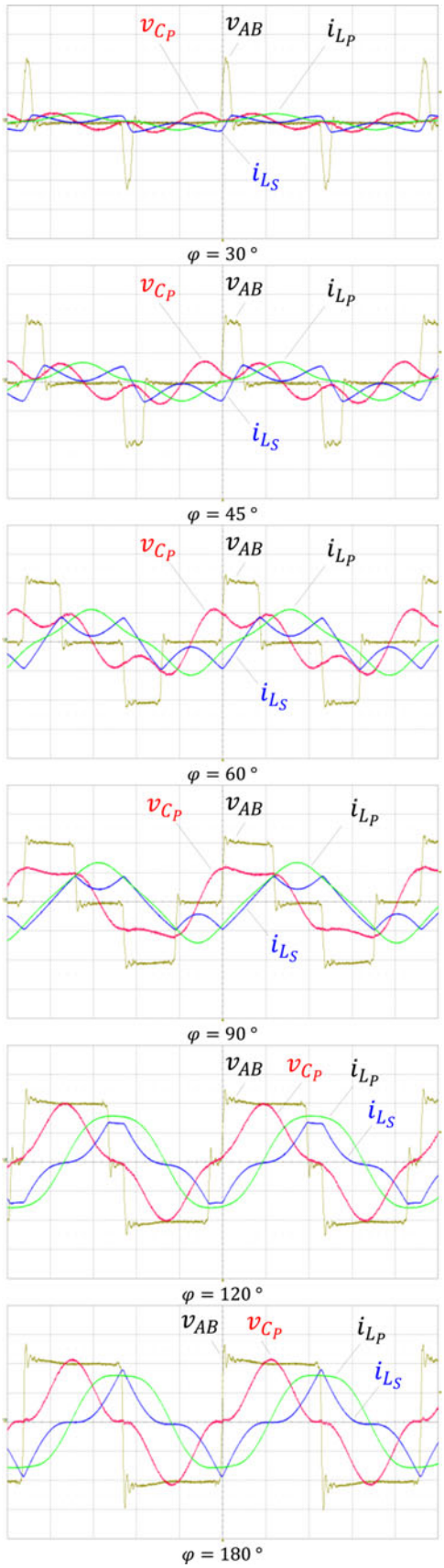

Fig. 24. Experimental waveforms of proposed auxiliary for various φ values at $\gamma = 1$, $V_{\rm in} = 200$ V. (100 V/div and 5 A/div): (a) $\varphi = 30°$. (b) $\varphi = 45°$. (c) $\varphi = 60°$ $\varphi = 90°$. (d) $\varphi = 120°$. (e) $\varphi = 180°$.

The relative difference between $I_{L_S\_0}$ of (34) and the average of auxiliary current during $t_{\rm transition}$ is denoted by $\Delta\,|I_{L_S\_0}|$ and studied numerically. Fig. 23(a) illustrates the percentage of $\Delta\,|I_{L_S\_0}|$ versus the percentage of $t_{\rm transition}/\,(T/2)$. With a longer $t_{\rm transition}$, the effective available auxiliary current becomes smaller. Therefore, Fig. 23(a) can used as the correction factor during the design process by selecting a higher $I_{L_S\_0}$ accordingly. Fig. 23(b) shows that the effect of $t_{\rm transition}$ is not the same for different phase shifts. The design process requires another step after selecting L in the previous section as follows: the range of φ variation is determined from (9) using the extremes of $V_{\rm in}$ from the specifications. Also the selected t_d is assumed as the upper bound of $t_{\rm transition}$; therefore, Fig. 23(b) specifies the largest $\Delta\,|I_{L_S 0}|$ to consider in updating the selected L in the previous section. The last step is to find C from (18).

V. Experimental Results

Experimental verification of the merits of the proposed auxiliary is provided in this section. The examined auxiliary circuit included $L = 11$ μH and $C = 30$ nF. The selected components for the converter are listed in Table II. The deadtime was 200 ns and the switches were STW69N65M5 with Rds(on) of < 90 mΩ in warm state (110 °C junction temperature) and the effective drain–source capacitance of 540 pF. MOSFET drivers were FOD3180.

To have a fair comparison between the baseline converter and the proposed one with the resonant auxiliary circuit, the transformer should be kept identical, so the effect of auxiliary circuits on the performance can be identified objectively. As shown in Section III, in (41), L_m should be equal to $2L$; therefore, the baseline converter tests were done by disconnecting C_P from node *M* defined in Fig. 5. The transformer is designed to be close to an ideal transformer (values listed in Table II).

Fig. 24 shows experimental waveforms of the resonant auxiliary for various phase shift values at $V_{\rm in} = 200$ V. Due to linearity of the auxiliary circuit, the behavior of the circuit can be known by testing at one $V_{\rm in}$ level.

Fig. 25 depicts the waveforms of the baseline and resonant auxiliaries for $\gamma = 1$ and $\varphi \leq 90°$. In all the cases, for a similar φ, the resonant auxiliary has a greater $I_{L_S\_0}$ value compared to $I_{L_m\_0}$ of the baseline converter, in full agreement with the prediction in Fig. 9 for $\varphi \leq 90°$. Fig. 26 shows the waveforms of the baseline and resonant auxiliaries for $\gamma = 1$ and $\varphi \leq 90°$. Again for a similar φ, the resonant auxiliary has a lower $I_{L_S\_0}$ value compared to $I_{L_m\_0}$ of the baseline converter in full agreement with the prediction in Fig. 9 for $\varphi \geq 90°$. For $\gamma = 1$ and $\varphi \geq 90°$, we have $I_{L_S\_0} = I_{L_m\_0}$ as expected.

The smoothness of rising edge and absence of strong voltage spikes in $v_{\rm AB}$ reveal the effectiveness of both approaches in maintaining ZVS turn on for leading and lagging legs. This proves that there is no difference in functionality between the two as far as ZVS is concerned. And the proposed resonant auxiliary has the same ZVS function with a lower rms current.

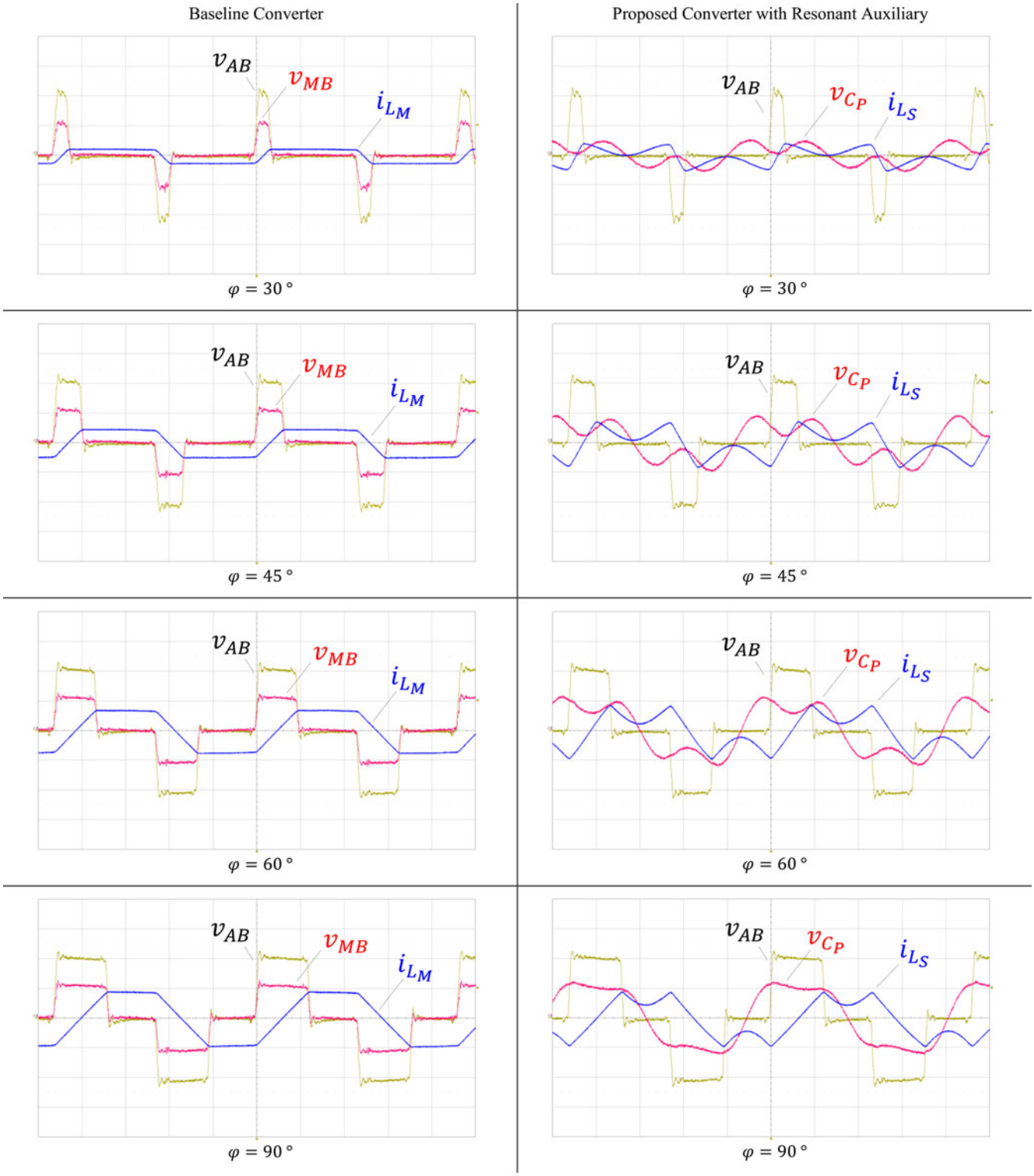

Fig. 25. Experimental waveforms of baseline (left) and resonant auxiliary (right) waveforms for $\gamma = 1$ and $\varphi \leq 90°$ $V_{\text{in}} = 200$ V (100 V/div and 5 A/div).

The impact of the auxiliary circuit choices on the efficiency of the prototype converter (including the control and gate driver circuits) is depicted in Fig. 27, for two V_{in} extreme levels of 200 and 300 V. First the efficiency was measures for various load levels without any auxiliary circuit. Then the baseline structure was tested that was capable of reducing the switching losses more than the additional conduction losses introduced in the circuit so the efficiency improved for all the load levels. The test results of proposed resonant auxiliary showed that efficiency improvement was more effective for lower load levels compared

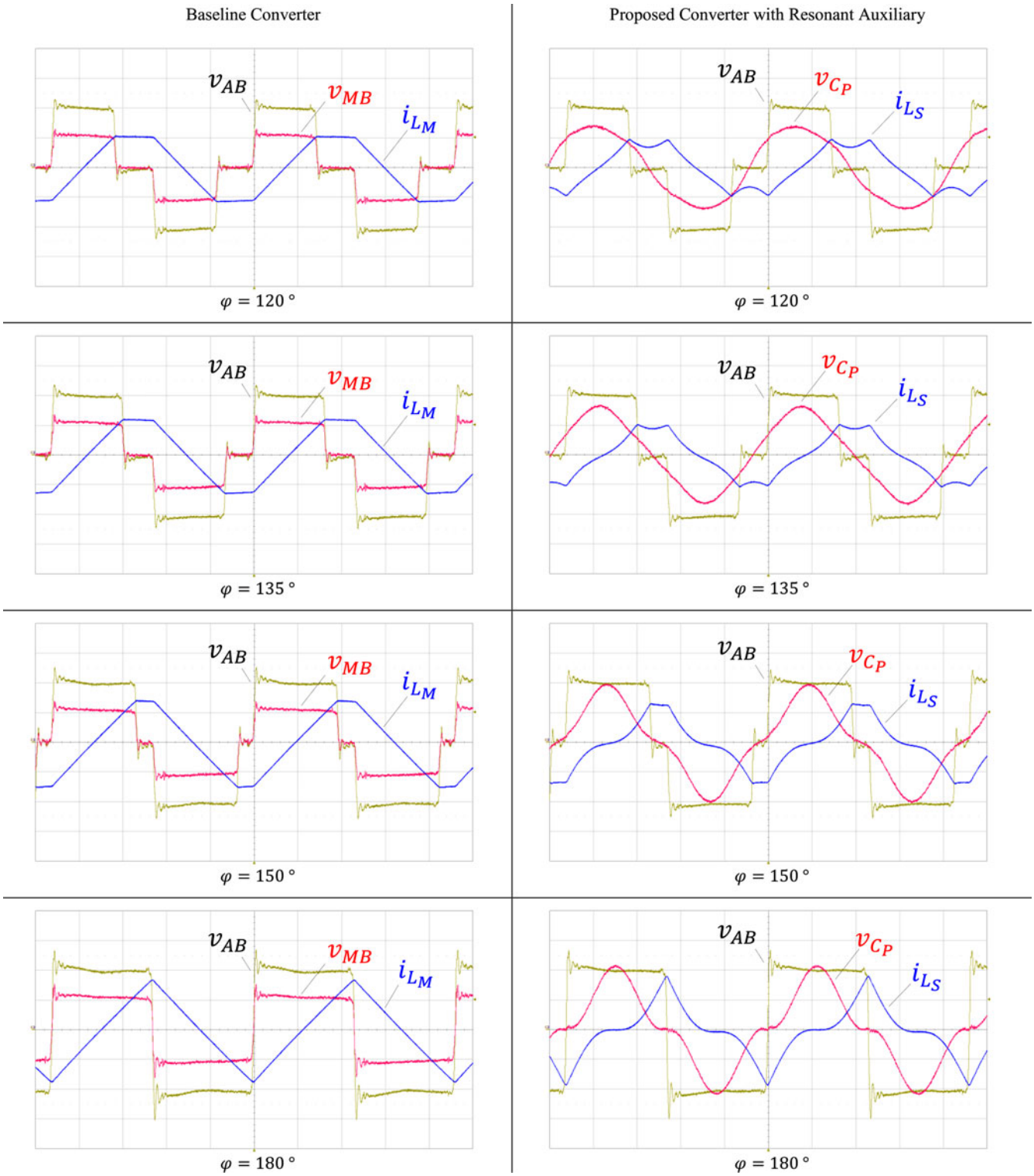

Fig. 26. Experimental waveforms of baseline (left) and resonant auxiliary (right) waveforms for $\gamma = 1$ and $\varphi \geq 90°$ $V_{\text{in}} = 200$ V (100 V/div and 5 A/div).

with heavy-load situations. Above 70% load, the conduction losses were dominant and the difference between two types of the auxiliaries became negligible.

Although the proposed resonant auxiliary is capable of providing the same functionality with lower rms current and sharper frequency dependence, there are some consequences such as a slightly higher component count, and the need to design the auxiliary inductors well below the saturation level of their cores. Also the design requires low ESR and ESL components in the resonant auxiliary due to the higher harmonic content in the auxiliary current. Also, the interface between the dc-side capacitor(s) and the switches should be designed carefully to minimize

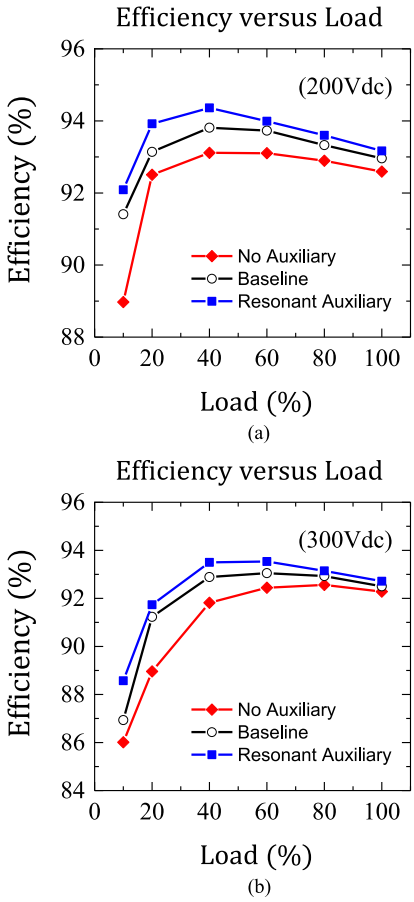

Fig. 27. Efficiency curves in absence of auxiliary circuit, the baseline converter and with the proposed resonant auxiliary circuits for $V_{\rm in}$ of (a) 200 V and (b) 300 V.

the parasitic stray inductance. A laminated bus bar structure is recommended.

VI. Conclusion

A simple passive auxiliary circuit is proposed to obtain ZVS operation of switches for the entire operational conditions of the phase shift full-bridge converter. Compared to the a baseline converter, which has a finite inductance parallel to the primary of the transformer to obtain ZVS, the proposed solution provides ZVS operation with the same peak and at least 20% lower rms auxiliary current. The details of auxiliary circuit operation and design procedure are described. An adaptive control approach is introduced to adjust the auxiliary current by varying the switching frequency up to 10% based on the average of input voltage. Experimental results confirm the effectiveness of the proposed circuit in providing the peak auxiliary current with lower rms values and up to 1% increase in efficiency.

References

[1] B. Y. Chen and Y. S. Lai, "Switching control technique of phase-shifted controlled full-bridge converter to improved efficiency under light-load and standby conditions without additional auxiliary components," *IEEE Trans. Power Electron.*, vol. 25, no. 4, pp. 1001–1012, Apr. 2010.

[2] G. Koo, G. Moon, and M. Yoon, "New zero-voltage switching phase-shift full-bridge converter with low conduction losses," *IEEE Trans. Ind. Electron.*, vol. 52, no. 1, pp. 228–235, Feb. 2005.

[3] B. P. McGrath, D. G. Holmes, P. J. McGoldrick, and A. D. McIver, "Design of a soft-switched 6-kW battery charger for traction applications," *IEEE Trans. Power Electron.*, vol. 22, no. 4, pp. 1136–1144, Jul. 2007.

[4] J. A. Sabate, V. Vlatkovic, R. B. Ridley, F. C. Lee, and B. Cho, "Design considerations for high-voltage high-power full-bridge zero-voltage-switched PWM converter," in *Proc. IEEE APEC. Rec.*, Mar. 11–16, 1990, pp. 275–284.

[5] P. K. Jain, W. Kang, H. Soin, and Y. Xi, "Analysis and design considerations of a load and line independent zero voltage switching full bridge DC/DC converter topology," *IEEE Trans. Power Electron.*, vol. 17, no. 5, pp. 649–657, Sep. 2002.

[6] J. G. Cho, J.-W. Baek, D. W. Yoo, H. S. Lee, and G.-H. Rim, "Novel zero-voltage and zero-current-switching (ZVZCS) full bridge PWM converter using transformer auxiliary winding," in *Proc. IEEE APEC Rec.*, Jun. 22–27, 1997, vol. 1, pp. 227–232.

[7] J. G. Cho, J.-W. Baek, C.-Y. Jeong, D. W. Yoo, H. S. Lee, and K.-Y. Joe, "Novel zero-voltage and zero-current-switching full bridge PWM converter using transformer auxiliary winding," *IEEE Trans. Power Electron.*, vol. 15, no. 2, pp. 250–257, Mar. 2000.

[8] J. G. Cho, J.-W. Baek, C.-Y. Jeong, and G.-H. Rim, "Novel zero-voltage and zero-current-switching full-bridge PWM converter using a simple auxiliary circuit," *IEEE Trans. Ind. Appl.*, vol. 35, no. 1, pp. 15–20, Jan./Feb. 1999.

[9] B. Gu, J.-S. Lai, N. Kees, and C. Zheng, "Hybrid-switching full-bridge DC–DC converter with minimal voltage stress of bridge rectifier, reduced circulating losses, and filter requirement for electric vehicle battery chargers," *IEEE Trans. Power Electron.*, vol. 28, no. 3, pp. 1132–1144, Mar. 2013.

[10] J. Cho, C. Jeong, and F. C. Lee, "Zero-voltage and zero-currents witching full-bridge PWM converter using secondary active clamp," *IEEE Trans. Power Electron.*, vol. 13, no. 4, pp. 601–607, Jul. 1998.

[11] E. Adib and H. Farzanehfard, "Analysis and design of a zero-current switching forward converter with simple auxiliary circuit," *IEEE Trans. Power Electron.*, vol. 27, no. 1, pp. 144–150, Jan. 2012.

[12] J. Dudrik, M. Bodor, and M. Pastor, "Soft-switching full-bridge PWM DC–DC converter with controlled output rectifier and secondary energy recovery turn-off snubber," *IEEE Trans. Power Electron.*, vol. 29, no. 8, pp. 4116–4125, Aug. 2014.

[13] Y. Jang and M. M. Jovanovic, "A new family of full-bridge ZVS converters," *IEEE Trans. Power Electron.*, vol. 19, no. 3, pp. 701–708, May 2004.

[14] Y. Jang, M. M. Jovanovic, and Y.-M. Chang, "A new ZVS-PWM full-bridge converter," *IEEE Trans. Power Electron.*, vol. 18, no. 5, pp. 1122–1129, Sep. 2003.

[15] S. J. Jeon and G. H. Cho, "A zero-voltage and zero-current switching full bridge DC–DC converter with transformer isolation," *IEEE Trans. Power Electron*, vol. 16, no. 5, pp. 573–580, Sep. 2001.

[16] X. Wu, J. Zhang, X. Xie, and Z. Qian, "Analysis and optimal design considerations for an improved full bridge ZVS DC–DC converter with high efficiency," *IEEE Trans. Power Electron.*, vol. 21, no. 5, pp. 1225–1234, Sep. 2006.

[17] M. Borage, S. Tiwari, S. Bhardwaj, and S. Kotaiah, "A full-bridge DC–DC converter with zero-voltage-switching over the entire conversion range," *IEEE Trans. Power Electron*, vol. 23, no. 4, pp. 1743–1750, Jul. 2008.

[18] I.-O. Lee and G. W. Moon, "Soft-Switching DC/DC converter with a full ZVS range and reduced output filter for high-voltage applications," *IEEE Trans. Power Electron*, vol. 28, no. 1, pp. 112–122, Jan. 2013.

[19] B. Gu, C.-Y. Lin, B. Chen, J. Dominic, and J.-S. Lai, "Zero-voltage-switching PWM resonant full-bridge converter with minimized circulating losses and minimal voltage stresses of bridge rectifiers for electric vehicle battery chargers," *IEEE Trans. Power Electron*, vol. 28, no. 10, pp. 4657–4667, Oct. 2013.

[20] Y.-F. Huang; C.-W. Liu, and Y. Konishi, "Soft-switching PWM full-bridge DC–DC converter with energy recovery transformer and auxiliary passive lossless snubbers," in *Proc. IEEE INTELEC Rec.*, Sep. 30–Oct. 4, 2007, pp. 622–627.

[21] M. Borage, S. Tiwari, and S. Kotaiah, "A passive auxiliary circuit achieves zero-voltage-switching in full-bridge converter over entire conversion range," *IEEE Power Electron. Lett.*, vol. 3, no. 4, pp. 141–143, Dec. 2005.

[22] A. Mousavi, P. Das, and G. Moschopoulos, "A novel ZCS-PWM full-bridge converter with a simple active auxiliary circuit," in *Proc. IEEE APEC Rec.*, Feb. 5–9, 2012, pp. 1273–1277.
[23] J. G. Cho, J. A. Sabate, and F. C. Lee, "Novel full bridge zero-voltage-transition PWM DC/DC converter for high power applications," in *Proc. IEEE APEC Rec.*, Feb 13–17, 1994, vol. 1, pp. 143–149.
[24] Z. Chen, S. Liu, and L. Shi, "Improved zero-voltage-switching pulse width modulation full bridge converter with self-regulating auxiliary current," *IET Power Electron.*, vol. 6, no. 2, pp. 287–296, Feb. 2013.
[25] A. F. Bakan, N. Altintas¸, and I. Aksoy, "An improved PSFB PWM DC–DC converter for high-power and frequency applications," *IEEE Trans. Power Electron*, vol. 28, no. 1, pp. 64–74, Jan. 2013.
[26] H. Daneshpajooh, M. Pahlevaninezhad, P. Jain, and A. Bakhshai, "An efficient soft switched DC–DC converter for electric vehicles," in *Proc. IEEE APEC Rec.*, Mar. 17–21, 2013, pp. 1798–1803.
[27] M. Pahlevaninezhad, J. Drobnik, P. Jain, and A. Bakhshai, "A load adaptive control approach for a zero voltage switching dc/dc converter used for electric vehicles," *IEEE Trans. Ind. Electron*., vol. 59, no. 2, pp. 920–933, Feb. 2012.
[28] A. Safaee, P. Jain, and A. Bakhshai, "An adaptive ZVS full bridge DC–DC converter with reduced conduction losses and frequency variation range," *IEEE Trans. Power Electron.*, Sep. 2014.
[29] A. Safaee, P. Jain, and A. Bakhshai, "A passive auxiliary circuit for load and line independent zero voltage switching in full bridge converters with reduced conduction losses for transportation applications," in *Proc. IEEE ITEC Rec.*, Jun. 2014, pp. 14–19.
[30] A. Safaee, P. Jain, and A. Bakhshai, "A low-RMS-current passive auxiliary circuit for ZVS operation of full bridge converters," in *Proc. IEEE ECCE Rec.*, Sep. 14–18, 2014, pp. 5065–5070.
[31] Z. Chen, S. Liu, and L. Shi, "A soft switching full bridge converter with reduced parasitic oscillation in a wide load range," *IEEE Trans. Power Electron.*, vol. 29, no. 2, pp. 801–811, Feb. 2014.
[32] F. Krismer, "Modeling and optimization of bidirectional dual active bridge DC–DC converter topologies," Ph.D. dissertation, Dept. Elect. Computer Eng., ETH Zurich, Zurich, Switzerland, 2010.

Alireza Safaee (S'08–M'12–SM'14) received the B.Sc. degree in electrical engineering from the Isfahan University of Technology, Isfahan, Iran, the M.Sc. degree in physics from the Sharif University of Technology, Tehran, Iran, the Ph.D. degree in engineering from the University of Quebec, Chicoutimi, QC, Canada, and the second Ph.D. degree in power electronics from Queen's University, Kingston, ON, Canada, in 1997, 1999, 2009, and 2015, respectively.

From 1997 to 2005, he was a Design Engineer and later a Design Manager at Manabe Taghzyeh Electronic Company, Tehran, Iran, where his teams developed several types of chargers, inverters, stabilizers, and UPS systems for more than 1000 communication sites and power plants. From 2011 to June 2014, he was an Electrical Analyst at Bombardier Transportation. He is currently a Principal Power Electronics Engineer at OSRAM Sylvania, Danvers, MA, USA. His research interests include power electronics, magnetic design, resonant and soft-switching converters, and their control methods toward applications in aviation and renewable energy systems.

Praveen Jain (S'86–M'88–SM'91–F'02) is currently a Professor of electrical and computer engineering at Queen's University, Kingston, ON, Canada, the Tier 1 Canada Research Chair in Power Electronics, and the Director of the Queen's Centre for Energy and Power Electronics Research. He made pioneering contributions in introducing resonant power conversion technology in telecommunications during his work at Nortel in the 1990s. He played a key role in the design and development of high-frequency power conversion equipment for the International Space Station at Canadian Astronautics in the late 1980s. Over the past 30 years, he has made sustained contributions to the theory and practice of power electronics through his considerable work with industry, including Astec, Freescale, General Electric, Intel, and Nortel. He is the Founder of two successful start-up companies, CHiL Semiconductor in the area of digital power controller (acquired by International Rectifier), and SPARQ Systems in the area of photovoltaic microinverters. He has published more than 450 papers and holds 50 patents.

He has supervised and guided more than 85 graduate students, postdoctoral fellows, and power electronics engineers who are well placed in industry and academia. Among his many awards and honors, he received the Queen's Prize for Excellence in Research, the IEEE William Newell Power Electronics Award, and became an IEEE IAS Distinguished Lecturer, a Fellow of the Royal Society of Canada, a Fellow of the Engineering Institute of Canada, a Fellow of the Canadian Academy of Engineering, and received the Engineering Medal of the Professional Engineers of Ontario.

Alireza Bakhshai (M'04–SM'99) received the B.Sc. and M.Sc. degrees from the Isfahan University of Technology, Isfahan, Iran, in 1984 and 1986, respectively, and the Ph.D. degree from Concordia University, Montreal, QC, Canada, in 1977.

From 1986 to 1993 and from 1998 to 2004, he was in the faculty of the Department of Electrical and Computer Engineering, Isfahan University of Technology. From 1997 to 1998, he was a Postdoctoral Fellow with Concordia University. He is currently at the Department of Electrical and Computer Engineering, Queen's University, Kingston, ON, Canada. His research interests include high-power electronics and applications in distributed generation and wind energy, control systems, and flexible ac transmission services.